Joule

CellPress

Article

Ni-Substituted Sr(Ti,Fe)O_3 SOFC Anodes: Achieving High Performance via Metal Alloy Nanoparticle Exsolution

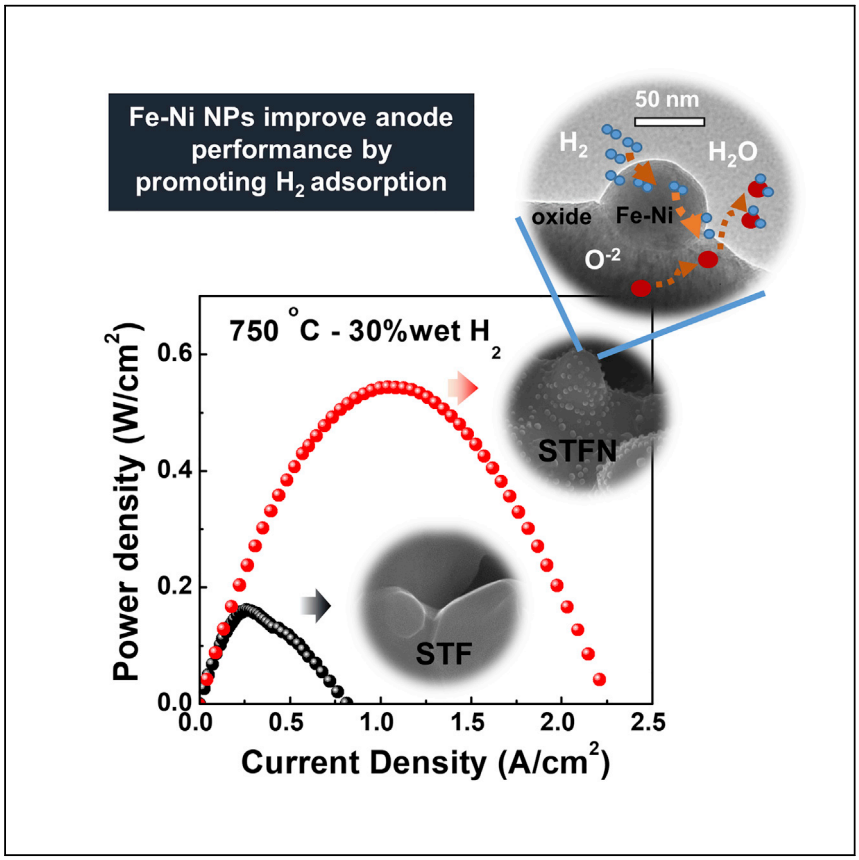

Ni-Fe nanoparticles are observed to exsolve from Ni-substituted $Sr_{0.95}(Ti_{0.3}Fe_{0.63}Ni_{0.07})O_{3-\delta}$ anode. The exsolved nanoparticles act to enhance hydrogen dissociative adsorption, yielding much lower anode polarization resistance and higher cell performance, especially under low pH_2 and temperatures, which is comparable with the current Ni-based cermets.

Tenglong Zhu, Horacio E. Troiani, Liliana V. Mogni, Minfang Han, Scott A. Barnett

hanminfang@mail.tsinghua.edu.cn (M.H.)
s-barnett@northwestern.edu (S.A.B.)

HIGHLIGHTS

Direct experimental comparison of oxide electrode with and without nanoparticles

Direct observation of improved cell performance under low pH_2 and temperature

Multiple measurement methods for exsolved nanoparticle alloy composition

First detailed thermodynamic theory explaining the metallic phase exsolution

Zhu et al., Joule 2, 1–19
March 21, 2018
https://doi.org/10.1016/j.joule.2018.02.006

Please cite this article in press as: Zhu et al., Ni-Substituted Sr(Ti,Fe)O_3 SOFC Anodes: Achieving High Performance via Metal Alloy Nanoparticle Exsolution, Joule (2018), https://doi.org/10.1016/j.joule.2018.02.006

Joule

CellPress

Article

Ni-Substituted Sr(Ti,Fe)O_3 SOFC Anodes: Achieving High Performance via Metal Alloy Nanoparticle Exsolution

Tenglong Zhu,[1,4] Horacio E. Troiani,[2] Liliana V. Mogni,[2] Minfang Han,[3,*] and Scott A. Barnett[1,5,*]

SUMMARY

Electrically conducting oxides have been proposed as alternatives to Ni-based cermet anodes for solid oxide fuel cells (SOFCs) to overcome issues such as coking and impurity poisoning, but their electrochemical performance is typically inferior to that of Ni-based cermets. Here we show that a new oxide composition, $Sr_{0.95}(Ti_{0.3}Fe_{0.63}Ni_{0.07})O_{3-\delta}$, yields anode polarization resistance competitive with Ni cermets, and substantially better than that of the corresponding Ni-free compound, $SrTi_{0.3}Fe_{0.7}O_{3-\delta}$. Exposure to fuel results in exsolution and nucleation of $Ni_{0.5}Fe_{0.5}$ nanoparticles uniformly dispersed on the Ni-substituted perovskite surface, whereas no nanoparticles are observed on $SrTi_{0.3}Fe_{0.7}O_{3-\delta}$. A general thermodynamic model is developed that quantitatively predicts exsolved nanoparticle composition. The reduction in anode polarization resistance by the nanoparticles, by as much as 4 times, is most pronounced at cell operating temperatures below 800°C and low H_2 partial pressures, suggesting that the nanoparticles improve performance by promoting H_2 adsorption.

INTRODUCTION

Ni-cermet fuel electrodes provide very good electrochemical activity (i.e., low electrode polarization resistance $R_{P,A}$), such that they are the preferred choice in conventional H_2-fueled solid oxide fuel cells (SOFCs). However, SOFCs with alternative anodes that minimize carbon deposition (coking), poisoning by fuel impurities, and degradation by redox cycling would enable direct utilization of real fuels such as natural gas and higher hydrocarbons.[1–4] The resulting power plant simplifications and cost reduction could be disruptive for SOFC technology through reduction or elimination of (1) fuel impurity removal components, (2) inert-gas purging hardware used to avoid anode redox cycles during plant shutdown,[5] (3) external fuel reformer and water boiler (or anode gas recycle pump), and (4) stack cooling (air blower) requirements due to endothermic on-anode hydrocarbon reforming.[6] There has been considerable activity in developing alternative conducting-oxide anode materials.[3,5,7–24] Early reports focused on doped chromite and titanate-based perovskites. These oxides, such as (La,Sr)CrO_3, and (Sr,La)TiO_3, are stable and have acceptable electronic conductivity with appropriate doping under SOFC fuel conditions. Although they can avoid the aforementioned problems with hydrocarbon fuels, the $R_{P,A}$ is generally much higher than typical Ni-based electrodes, leading to low cell power density. One strategy shown to improve performance is substitution of a large fraction of a reducible transition-metal cation on the B site, resulting in substantial oxygen vacancy concentrations and enhancement of oxygen ionic conductivity. These mixed ionically and electronically conducting (MIEC) oxide

Context & Scale

Mixed conducting perovskite oxides are proposed as alternatives for solid oxide fuel cell anodes, and *in situ* metallic nanoparticle precipitation/exsolution is considered to improve their performance. However, understanding of exsolution is still lacking, such as the reason why specific cations exsolve from an oxide anode and what determines the exsolved phase composition under various anode conditions. Here we directly compare Sr(Ti,Fe)O_3-based anodes with and without exsolved metallic nanoparticles, showing their impact on electrochemical characteristics especially under low anode hydrogen concentrations and low temperatures. Three different methods are used to quantitatively determine the composition of the exsolved (Ni,Fe) nanoparticles, and for the first time demonstrate that this can be achieved through thermogravimetric analysis. This work is the first to propose a detailed thermodynamic theory predicting the exsolved nanoparticle composition with successful experimental verification.

anodes (e.g., $Sr_2Mg_{1-x}Mn_xMoO_{6-\delta}$, $PrBaMn_2O_{5+\delta}$, $(PrBa)_{0.95}(Fe_{0.9}Mo_{0.1})_2O_{5+\delta}$, and $La_{1-x}Sr_xCr_{1-x}Fe_xO_{3-\delta}$) have indeed shown reduced $R_{P,A}$ values, presumably because fuel oxidation can occur on the entire oxide surface. For example, cells with $SrTi_{0.3}Fe_{0.7}O_{3-\delta}$ (STF)-based anodes[21,24] have shown $R_{P,A}$ values as low as 0.13 $\Omega \cdot cm^2$ at 800°C in humidified hydrogen. However, $R_{P,A}$ is often observed to increase rapidly with decreasing temperature and H_2 partial pressure; it was suggested that this was due to a rate limitation by H_2 dissociative adsorption, since there is no metallic catalyst to promote hydrogen dissociation.[21]

The introduction of nanoscale metallic catalyst particles onto oxide anode surfaces has been shown to reduce $R_{P,A}$ values. There have been a number of reports of catalyst particles being produced by wet-chemical infiltration.[25,26] On the other hand, exsolution of reducible cations from oxide anodes, upon exposure to fuel, has been shown to yield well-dispersed metallic nanoparticles. This method may have advantages compared with infiltration: (1) no extra process steps are required; (2) the catalyst particles can be substantially smaller and presumably more active than infiltrated particles[8,27,28]; (3) the catalyst material can be introduced selectively into the anode functional layer; (4) it is possible to regenerate the nanoparticles via a redox cycle[29]; and (5) the nanoparticles tend to be embedded into the oxide surface, which may discourage nanoparticle coarsening.[30] Since the initial report showing that Ru nanoparticles formed on $La_{0.8}Sr_{0.2}Cr_{0.82}Ru_{0.18}O_{3-\delta}$ anodes upon exposure to humidified hydrogen, reducing $R_{P,A}$,[8,31] there have been numerous reports of catalyst exsolution. Transition-metal cations including Fe, Co, Ni, Pd, and Ru have been exsolved from doped chromite and titanate anodes. In cases where the oxide contains two reducible metal cations, e.g., $(Pr/La)_{0.4}Sr_{0.6}Co_{0.2}Fe_{0.7}Nb_{0.1}O_{3-\delta}$, $La_{0.7}Sr_{0.3}Cr_{0.85}Ni_{0.1125}Fe_{0.0375}O_{3-\delta}$, and $LaNi_{0.6}Fe_{0.4}O_{3-\delta}$, exsolution results in Fe-Co or Fe-Ni alloy nanoparticle formation, although alloy composition has typically only been estimated.[32–35] Recent results indicate that the improved performance of $La_{0.8}Sr_{0.2}Cr_{0.82}Ru_{0.18}O_{3-\delta}$ anodes due to Ru nanoparticle formation can be quantitatively modeled by assuming that they accelerate the dissociative H_2 adsorption process.[21] Although most reports have featured tests with H_2 fuels, oxide anodes with exsolved metal nanoparticles have also been shown to provide good and stable performance with hydrocarbon fuels and to exhibit good tolerance to H_2S contaminant.[30,32–34,36] Finally, exsolved catalyst oxide fuel electrodes have shown promising performance in solid oxide steam electrolysis cells.[37,38]

It was recently shown in studies of the $(La_{1-x}Sr_x)(Cr_{0.3}Fe_{0.7-y}Ru_y)O_{3-\delta}$ system that the combination of an MIEC oxide with catalytic nanoparticles yields better anode performance than either alone.[22] Studies on titanate-based oxides have focused on transition-metal substitution to introduce MIEC character (STF anodes),[21,24] or substitutions that produce catalytic nanoparticles in (La,Sr)(Ti,Ni)O_3,[30,37–40] but not both together. Finally, while the aforementioned exsolution anodes provide good electrochemical performance, detailed comparisons of the electrochemical results with and without nanoparticles have not been made, such that the exact mechanisms whereby they enhance performance are not known.

In this study, we present results on $Sr_{0.95}(Ti_{0.3}Fe_{0.63}Ni_{0.07})O_{3-\delta}$ (STFN) anode materials designed to feature both MIEC properties and catalytic nanoparticles, and compare them with STF anodes. Sr-deficient STFN is utilized so that the perovskite phase approaches stoichiometry upon Ni exsolution; thus, by comparison with stoichiometric nanoparticle-free STF anodes, performance changes caused by the presence of exsolved nanoparticles are isolated. Electrode microstructure and exsolution behavior are described in detail, including nanoparticle composition verified

[1]Department of Materials Science and Engineering, Northwestern University, Evanston, IL 60208, USA

[2]CONICET-CNEA, Centro Atómico Bariloche, Avenida Bustillo 9500, CP 8400 S.C. Bariloche, Argentina

[3]Department of Energy and Power Engineering, Tsinghua University, Beijing 100084, China

[4]Present address: Nanjing University of Science and Technology, Nanjing, China

[5]Lead Contact

*Correspondence: hanminfang@mail.tsinghua.edu.cn (M.H.), s-barnett@northwestern.edu (S.A.B.)

https://doi.org/10.1016/j.joule.2018.02.006

Please cite this article in press as: Zhu et al., Ni-Substituted Sr(Ti,Fe)O_3 SOFC Anodes: Achieving High Performance via Metal Alloy Nanoparticle Exsolution, Joule (2018), https://doi.org/10.1016/j.joule.2018.02.006

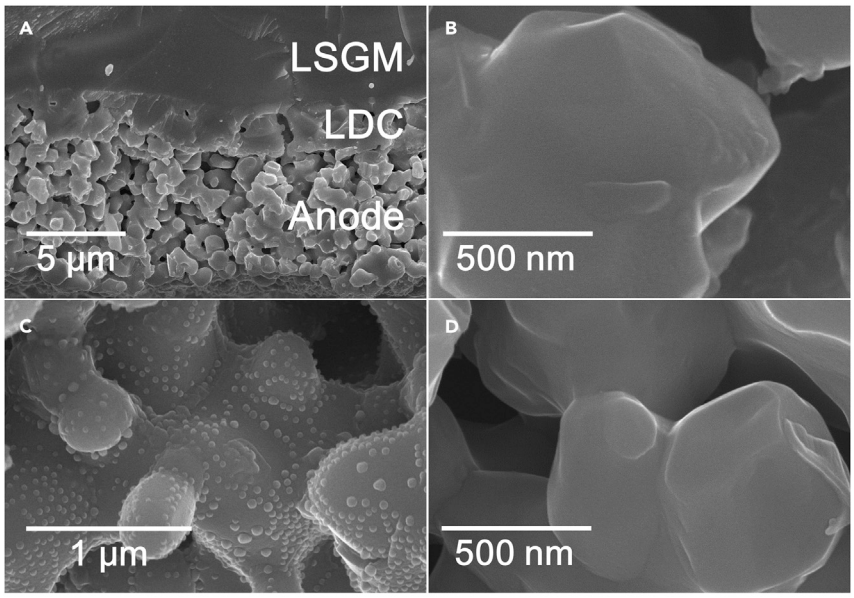

Figure 1. Scanning Electron Microscopy Images of Anode Microstructures
(A–D) STFN anode before reduction at low magnification (A) and higher resolution (B); STFN anode after cell test (C); STF after cell test (D).

using three independent measurements. A thermodynamic model is developed that predicts the Ni-Fe alloy composition as a function of anode fuel composition. Electrochemical characteristics of these anodes in $La_{0.8}Sr_{0.2}Ga_{0.83}Mg_{0.17}O_{3-\delta}$ (LSGM) electrolyte-supported cells are discussed including the role of the alloy nanoparticles, and it is shown that these anodes yield performance comparable with Ni-YSZ (yttria stabilized zirconia).

RESULTS

Characterization of the Exsolution Process

Figure 1A shows a low-magnification scanning electron microscopic image of an STFN anode. The thickness is ~10 μm. The porous microstructure shows a feature size of 2–3 μm, similar to that shown previously for STF anodes.[21] A higher-magnification view of the as-prepared STFN anode (Figure 1B) shows a clean smooth oxide surface, but after reduction in humidified H_2 at 850°C, nanoparticles with diameters of ~20–70 nm are observed uniformly distributed on the oxide surface (Figure 1C). The wide distribution of particle sizes presumably results from nucleation at different times during the exsolution process. For comparison, the STF anode shows a smooth featureless oxide surface both before and after cell testing; the latter case is shown in Figure 1D. As discussed further below, the presence of nanoparticles on STFN, and not STF, is not surprising because Ni is more readily reducible than Fe. The characterization of these nanoparticles and the oxides are discussed here, whereas the electrochemical response including the effect of exsolution is addressed later.

Figure 2A shows the weight loss of the STF and STFN powders during reduction at 850°C, upon switching the gas environment from a pO_2 of 2×10^{-4} atm (diluted in Ar) to an $H_2/Ar/H_2O$ mixture with an effective pO_2 of 5.9×10^{-20} atm. STF, used as a reference for comparison of the STFN data, loses ~0.5% of its mass within ~300 s, after which the mass remains stable. That is, STF is stable at this temperature and gas condition. This indicates a decrease in $3 - \delta$ from ~2.654 to 2.601, suggesting

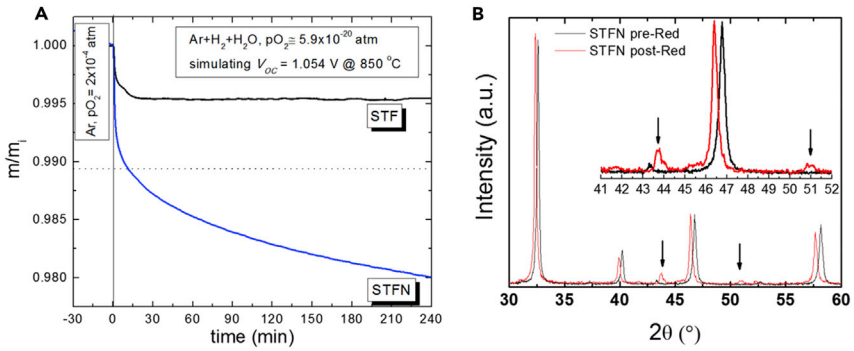

Figure 2. TG Plots and XRD Patterns for Powders

(A) Mass m normalized to initial mass m_i measured versus time at 850°C, for STF and STFN powders, upon changing the gas composition from 2 × 10^{-4} atm O_2 diluted in Ar to an H_2/Ar/H_2O mixture with an effective pO_2 of 5.9 × 10^{-20} atm.

(B) XRD patterns of the as-prepared STFN powder and after reduction in 30% H_2/67% Ar/3% H_2O at 850°C for 4 hr. The inset shows a magnified view of the Fe-Ni alloy peaks (arrows).

that the valence state of Fe changes from $Fe^{+3.01}$ initially in the Ar flux to $Fe^{+2.86}$ in the H_2/Ar/H_2O mixture. For STFN, the initial mass loss is similar, but then the mass continues to decrease throughout the entire reduction process. The additional mass loss can be explained in part by the reduction of Ni, presumably initially present as Ni^{+2} in STFN, to metallic Ni^0. The dotted line at m/m_i = 0.989 indicates the maximum mass loss that would be expected if Fe exhibits the same change in oxidation state as observed in STF, and all the Ni in STFN is reduced to the metallic state. Clearly the actual mass loss is higher, indicating that Fe is also being reduced to Fe^0. Assuming, for example, that the Fe in the oxide remains on average in the $Fe^{+2.86}$ state upon reduction, as in STF, and a fraction of the Fe exsolves and dissolves in the $Ni_{1-x}Fe_x$ alloy nanoparticles (Fe^0), the Fe fraction in the alloy can be estimated as x = 0.51 from the measured mass loss. The Fe-Ni exsolution also produces an excess of Sr in the remaining oxide, as discussed below.

Figure 2B compares the X-ray diffraction (XRD) patterns of STFN as-prepared powder—after calcination in air at 1,200°C for 10 hr—with the same powder after reduction in the above thermogravimetric (TG) experiment. This figure indicates that the pre-reduced (preRED) powder has a cubic perovskite structure (PDF#34-0641: $SrFeO_{3-x}$) with strong sharp diffraction peaks. No obvious secondary phases are detected, demonstrating that the pre-reduced compound is single phase within the sensitivity limit of XRD (~1%), despite an A-site deficiency of 5%. After reduction in 30% H_2/67% Ar/3% H_2O at 850°C for 4 hr (postRED), the XRD patterns indicate that the perovskite structure is maintained. The main peaks all shift to lower angle after reduction, with the larger lattice parameter caused by oxygen loss. However, new peaks are detected at ~47° and 51° (see inset). These peaks index well with fcc $Ni_{1-x}Fe_x$ alloy structure; as discussed further below, this phase forms by exsolution from the perovskite phase. The measured lattice parameter obtained from the average peak position (the average was used because of the significant noise in these broad low-intensity peaks from the minority nanoscale alloy) is ~3.576 Å, indicating x = 0.49 in $Ni_{1-x}Fe_x$ based on reported alloy lattice parameters.[41] When STFN is reduced under a slightly less reducing condition, 10% H_2/87% Ar/3% H_2O at 850°C for 3 hr, a slightly smaller lattice parameter of ~3.562 Å was obtained, indicating x = 0.28. The patterns for similarly reduced STF powder (data not shown)

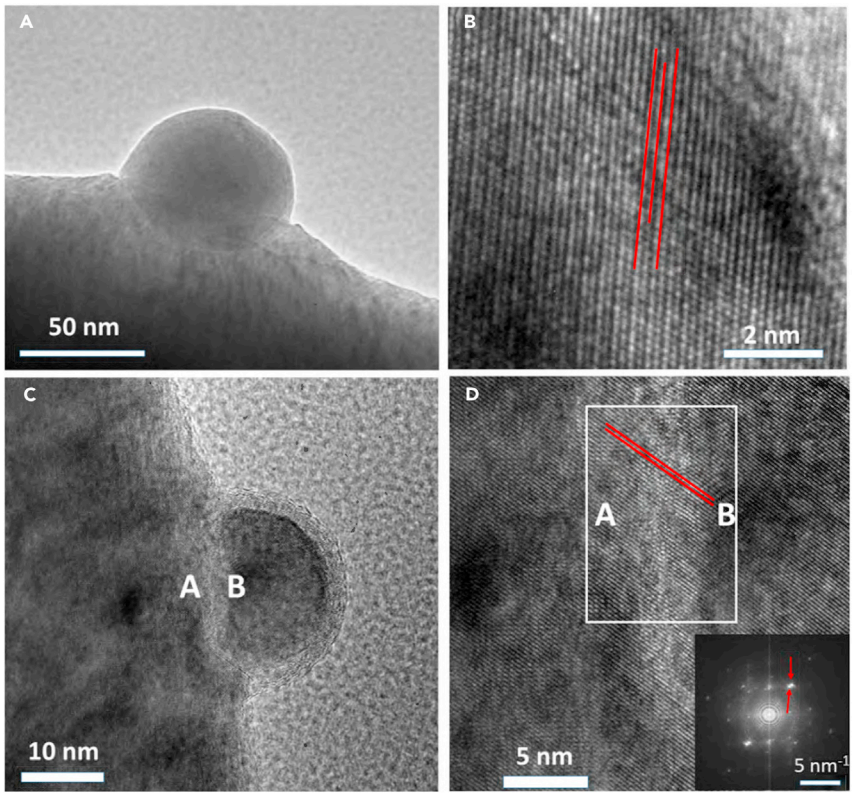

Figure 3. TEM Images

(A and B) A typical exsolved (Fe,Ni) nanoparticle on the STFN anode surface (A) and HRTEM image of the remaining perovskite (B) (EDS analysis is shown in Table 1). Red lines are a guide to the eye showing the transition from the unmodulated to the modulated zone.

(C and D) HRTEM image of an incipient nanoparticle (C) and a higher-magnification view of the perovskite-nanoparticle interface (D). The red lines indicate lattice planes, and the inset shows the FFT of the interface; the red arrows indicate the reflections corresponding to both sides of the interphase and the small mismatch between both phases.

are nearly identical to STFN, except that the reduced STF powder showed no secondary phase peaks, consistent with prior reports.[21,24]

Figure 3A shows a bright-field transmission electron microscopy (TEM) image of one of the larger exsolved nanoparticles on the oxide surface. The particle presents an approximately spherical free surface and is surrounded by an amorphous surface layer; a similar observation for exsolved Ni nanoparticles was explained by formation of a native oxide upon exposure of the anode to air.[28] Since the particles contain Fe, it is also possible that Fe becomes oxidized during cooling of the sample in the humidified H_2 fuel mixture after the TG test. The particle appears to be embedded into the perovskite surface, a shape that has been reported for exsolved Ni particles on $La_{0.52}Sr_{0.28}Ni_{0.06}Ti_{0.94}O_3$, and termed "socketing."[30] The perovskite phase in Figure 3A shows a mottled contrast that is not observed prior to reduction or in reduced STF. The reason for this can be seen in Figure 3B, which shows an high-resolution TEM (HRTEM) image of a typical region in the oxide within ~5 nm of the oxide surface after the exsolution process. Some regions (e.g., in the upper right) show uniform fringe contrast similar to that observed in reduced STF powder. In the region just below this, the fringe contrast is modulated, suggesting the formation of a layered structure, similar to those reported by Canales-Vázquez et al. for La-Sr titanates,[42] but with an

Table 1. Element Composition of the Exsolved Nanoparticles and the Oxide Bulk from TEM-EDS

Element	Oxide Composition	Nanoparticle Composition
	Atomic %	Atomic %
TiK	16	0
FeK	34	55
NiK	0	45
SrK	50	0
Total	100	100

The measured composition accuracy is ±1 at %.

apparent doubling of the lattice parameter. The red lines in the image highlight the lattice-fringe positions in the two regions. No obvious SrO-rich phases are observed in the TEM measurements, in agreement with the XRD results.

The nanoparticles observed by TEM are mainly in the 20- to 70-nm size range, in agreement with that observed by scanning electron microscopy (Figure 1). Figure 3C shows an HRTEM image of one of the smaller nanoparticles, where the oxide amorphous layer is seen more clearly. Figure 3D shows a higher-magnification view of the exsolved particle/oxide interface. The (111) fcc Fe-Ni atomic planes from the nanoparticle semi-coherently match the (111) atomic planes from the perovskite, despite the ~13% metal/oxide lattice mismatch. This is consistent with the fast Fourier transform (FFT) (inset in Figure 3D), where a double diffraction spot can be observed due to both matching structures. There is an apparent interface width of ~5 nm, indicated by lighter image contrast, presumably an artifact resulting from the projection of the curved oxide/metal interface.

Table 1 shows the results of energy dispersive spectroscopy for TEM (TEM-EDS) analysis of the particle shown in Figure 3A, showing that the nanoparticle contains only Fe and Ni, with $x = 0.55$ in $Ni_{1-x}Fe_x$. Note that the electron probe size in the TEM-EDS measurement was ~20 nm, small enough in comparison with the 60-nm particle to measure its composition with reasonable accuracy. The TEM-EDS Fe content is higher than the composition calculated from the XRD lattice parameter, $x = 0.49$, but the values are within the combined experimental errors. The difference may also be explained by the fact that TEM-EDS measures the local composition of a specific nanoparticle, whereas the XRD measures an average over many particles. The TEM-EDS results are in agreement with the value obtained from the TG data; the assumption made in this analysis, of complete Ni reduction, is verified by the TEM-EDS measurement that showed no Ni in the oxide. In summary, the estimated Fe content values in $Ni_{1-x}Fe_x$ are $x = 0.51$ from TG, $x = 0.49$ from XRD, and $x = 0.55$ from TEM. Therefore, it is a good approximation to assume the formation of $Ni_{0.5}Fe_{0.5}$ alloy nanoparticles during cell operation with V_{OC} = 1.054 V at 850°C. The measured perovskite composition from Table 1 is $Sr(Ti_{0.32}Fe_{0.68})O_{3-\delta}$, suggesting that the initial A-site deficiency of the STFN powder was reduced by exsolution.

Electrochemical Performance Test

Current-voltage characteristics of single cells with STF (Figures 4A and 4C) and STFN (Figures 4B and 4D) anodes are shown at different temperatures for anode H_2 partial pressures p_{H_2} = 0.97 atm and at various p_{H_2} at 750°C in Figure 4. Maximum power densities (P_{max}) at 850°C were similar in Figures 4A and 4B. However, the STFN-anode cell maintained its power density at lower temperature much better than the STF cell. For example, P_{max} for the STFN-anode cell dropped from 1.3 W

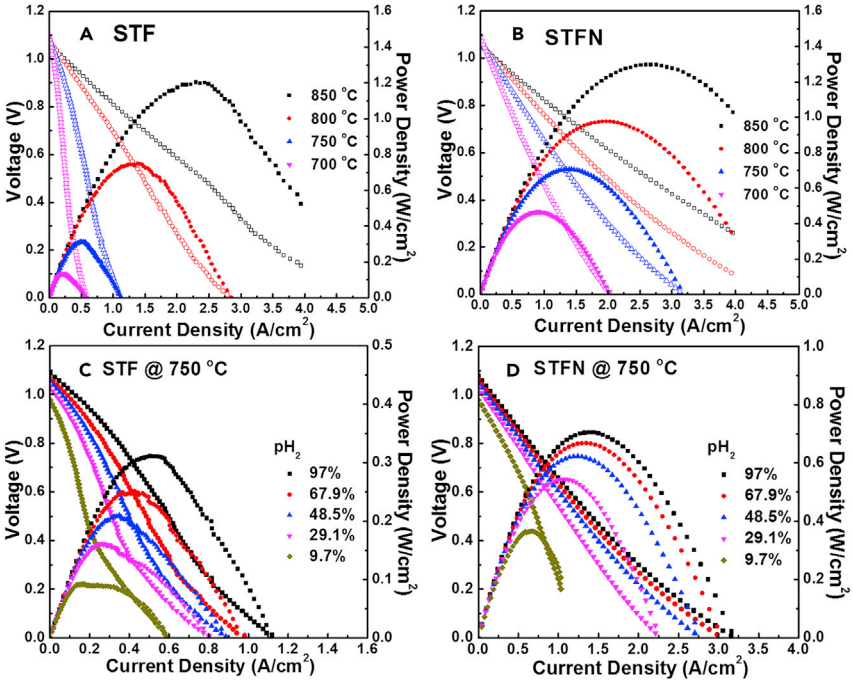

Figure 4. *j-V-P* Curves of STF- and STFN-Anode Cells

(A–D) Cell performance of STF (A) and STFN (B) anode cells under humidified H_2 at different temperatures, with anode fuel flux of 100 mL min^{-1} *j-V-P* curves of STF (C), and STFN (D) anode cell tested at 750°C under different H_2 partial pressures.

cm^{-2} at 850°C to 0.4 W cm^{-2} at 700°C, whereas P_{max} for the STF-anode cell from 1.1 W cm^{-2} at 850°C to 0.13 W cm^{-2} at 700°C. The p_{H_2} dependence in Figures 4C and 4D shows different behaviors for STFN and STF. First, P_{max} values are 2–4 times higher for STFN. For STFN, there is relatively little decrease in current density at a given cell voltage, at least until p_{H_2} is decreased below 0.29 atm. For STF, the decrease in current density with decreasing p_{H_2} is substantially larger. The current-voltage curves for STFN show positive curvature except at the lowest p_{H_2}. The negative curvature of the STF current-voltage curves was previously explained as a limiting current behavior due to a hydrogen adsorption limitation on STF anodes. The rapid increase in current density as the cell voltage decreases to zero, observed for STF, has also been observed previously.[21]

Figure 5 shows electrochemical impedance spectrum (EIS) scans taken at 800°C under various p_{H_2}, from cells with STF (Figure 5A) and STFN (Figure 5B) anodes. The cell with STFN anode had the lower overall resistance, consistent with its higher P_{max} values in the current-voltage results. The EIS data were fitted using an equivalent circuit model consisting of an inductor, a resistive element, and three RQ elements, the same as used previously to fit similar cells with STF anodes.[21,24] Figure 5C presents an example fit to data from an STFN-anode cell tested at 800°C and p_{H_2} = 0.291 atm. The fits with three RQ elements match well with the data; in general, it was not possible to obtain good fits to all the data with only two RQ elements.

The high-frequency intercepts in Figure 5, corresponding to the cell ohmic resistances, varied differently with p_{H_2} for the different anodes. For STFN cell, the resistance did not vary significantly with p_{H_2} and was as expected for the

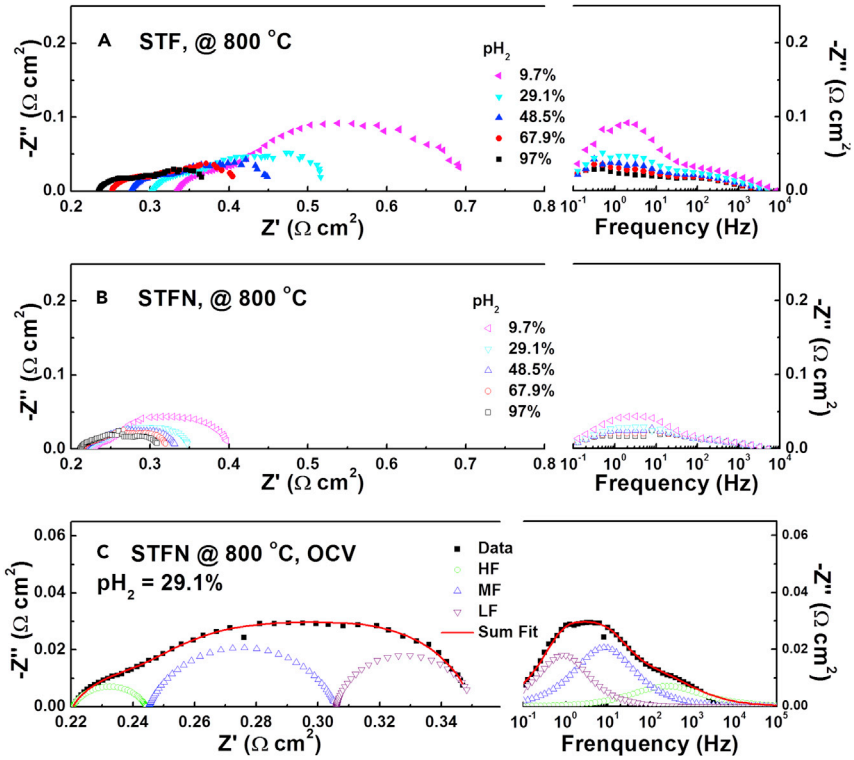

Figure 5. Electrochemical Impedance Spectrum

(A and B) Nyquist and Bode plots for the STF (A) and STFN (B) anode cells under various H_2 partial pressures (3% H_2O/H_2/Ar) at 800°C.

(C) Example fits to the EIS data of STFN-anode cell tested at 800°C under anode H_2 partial pressure of 29.1% at open-circuit voltage condition using an equivalent electrical circuit model.

0.3-mm-thick LSGM electrolyte, ~0.21 $\Omega \cdot cm^2$ at 800°C. For STF, the observed increase in ohmic resistance is attributed to a contribution from the oxide anode, as discussed previously.[21] These results indicate that the conductivity of STFN was higher than that of STF; although it has previously been suggested that exsolved metallic particles contribute significantly to the anode conductivity,[35,43] it does not appear that the present particles are percolated (Figure 1). The high-frequency responses in Figure 5, which did not vary with p_{H_2}, can be attributed to the cathode. The medium- and low-frequency response resistances increased with decreasing p_{H_2}, and hence they must be associated with anode processes. The medium- and low-frequency responses were difficult to separate quantitatively due to their similar maximum frequency. Thus, in the following discussion, the total of the medium- and low-frequency resistances, defined as the anode polarization resistance $R_{P,A}$, is used.

Figure 6A shows a plot of $R_{P,A}$ versus p_{H_2} for the STFN- and STF-anode cells. The $R_{P,A}$ values for STFN were lower than for STF, and the pressure dependence fit well to $R_{P,A} \propto (p_{H_2})^m$ with $m \sim 0.25$. This dependence is weaker than that observed for STF, with $m \sim 0.5$. This indicates a change in hydrogen oxidation mechanism, presumably due to the alloy nanoparticles. Figure 6B shows the $R_{P,A}$ values plotted versus inverse temperature, for cells with both anodes, at various p_{H_2}. None of the data can be fitted using a simple Arrhenius-type dependence. Activation energies estimated in different temperature ranges ranged from 39 to 56 kJ mol^{-1} for STF, higher than the range found for the STFN anode, 20–27 kJ mol^{-1} anode.

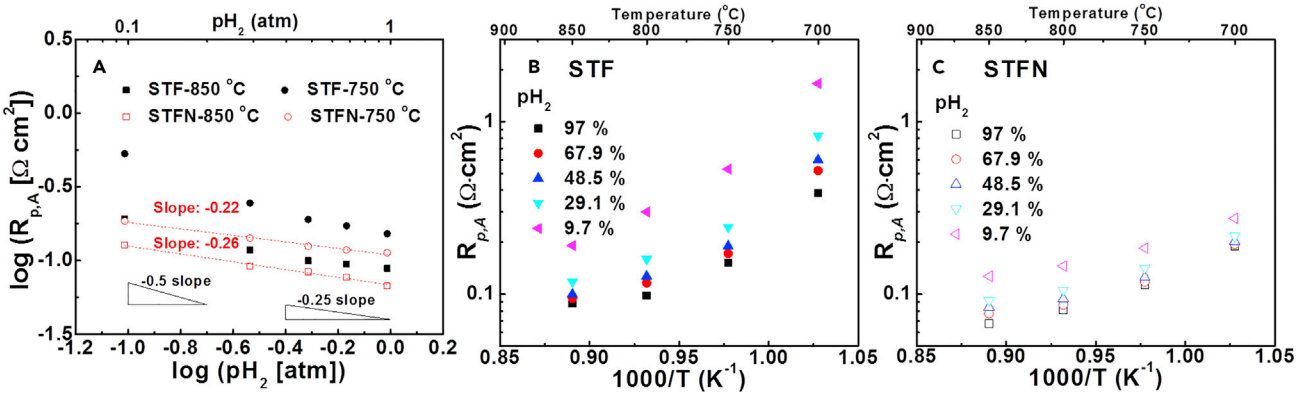

Figure 6. Anode Polarization Resistances

(A) Anode polarization resistance for the STF and STFN-anode cells, measured at 750 and 850°C, plotted versus p_{H_2}.

(B and C) Arrhenius plots of anode polarization resistances for the STF (B) and STFN (C) anode cells tested at various p_{H_2}.

These dependences contributed to the strong temperature dependence of cell power density in Figure 4.

To summarize the above results and highlight the effect of Ni substitution on cell performance, we have replotted selected *j*-V and EIS data from Figures 4 and 5 in Figures 7A–7D to directly compare cells with STF and STFN anodes. Results are shown at 850°C and 700°C, with p_{H_2} values of 0.97 and 0.29 atm. Note that both cells show the same open circuit voltage, i.e., V_{OC} = 1.054 V at 850°C and p_{H_2} = 0.97 atm. At 850°C and p_{H_2} = 0.97 atm, the STF and STFN cells showed similar performance (Figure 7A). Decreasing p_{H_2} to 0.29 atm at 850°C increased the resistance and decreased the current density for both cells, but more so for the STF-anode cell (Figure 7B). The differences between the cells becomes more pronounced at the lower temperature of 700°C. For example, the resistance of the STFN cell for p_{H_2} = 0.97 atm was 2.5 times lower than that of the STF-anode cell, and the current density at V = 0.7 V was 3.1 times higher (Figure 7C). For p_{H_2} = 0.29 atm and 700°C, the difference was even larger, with the resistance being 4 times lower and the current density 4.5 times higher for the STFN cell (Figure 7D).

Figure 7E shows the results of two preliminary life tests—one carried out in humidified H_2 (p_{H_2} = 0.97 atm) and the other in a humidified 50%:50% H_2/CO mixture. In both fuels, the cell voltage increased slightly during the first ~10 hr, and then remained reasonably constant or decreased slightly over 150–200 hr. This indicates that there was little or no coarsening of the Ni-Fe alloy nanoparticles that would otherwise deleteriously affect anode performance.[8,27]

The present STFN cells show performance among the best that have been reported for SOFCs with oxide anodes,[21,22,24,32,33,43] with a maximum power density at 800°C, in air and humidified hydrogen, of 0.95 W cm^{-2}, and anode polarization resistance of 0.081 Ω cm^2. Figure 7F shows a comparison of the measured $R_{P,A}$ values for STF and STFN at various temperatures, compared with values for Ni-YSZ anodes measured under the same conditions. Specifically, the Ni-YSZ values shown are the electrochemical portion (not including the gas diffusion contribution) of the anode impedance response obtained by fitting EIS data from high-quality anode-supported SOFCs (maximum power density of 1.3 W cm^{-2} at 800°C).[45] Note that the STFN and Ni-YSZ values are nearly identical, while STF is inferior, especially at lower temperature.

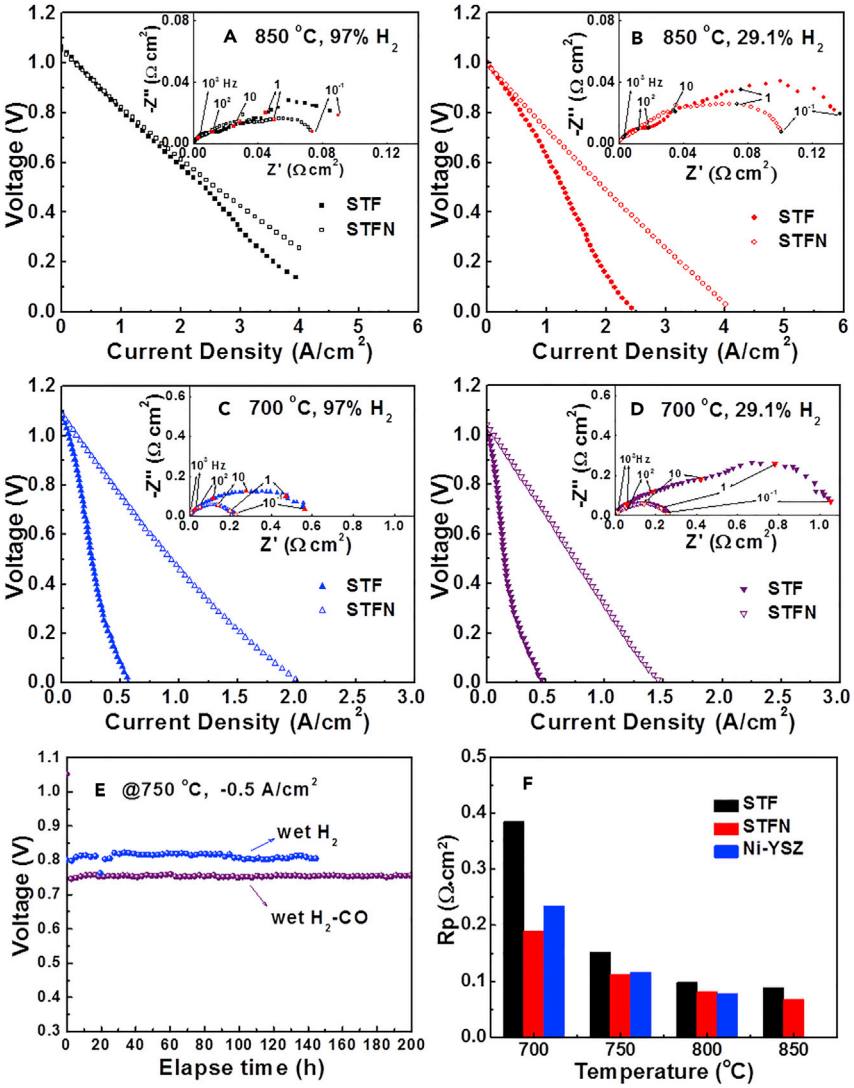

Figure 7. Cell Performance Comparison

(A–D) Comparison of *j*-*V* curves and EIS data from cells with STF and STFN anodes, measured at different temperatures and various anode H_2 partial pressures of (A) 850°C, 97% H_2, (B) 850°C, 29.1% H_2, (C) 700°C, 97% H_2, and (D) 700°C, 29.1% H_2. The fuel was humidified with about 3% H_2O and balanced with Ar, at a total flow rate of 100 mL min^{-1}. The high-frequency intercepts were set to zero in the EIS plot in order to facilitate comparison of the polarization arcs.

(E) Cell voltage versus time for STFN-anode cells at 750°C with air at the cathode and either humidified H_2 or humidified syngas (50% H_2/50% CO). The fuel flow rate is 60 mL min^{-1}.

(F) Anode polarization resistances for the STF and STFN-anode cells compared with Ni-YSZ anode cell,[44] measured at p_{H_2} = 97%, plotted versus temperature.

DISCUSSION

Metal Alloy Exsolution

The present results are similar to a number of prior reports showing exsolution of catalyst nanoparticles.[8,27,28] While most of the prior results suggested exsolution of elemental metal nanoparticles,[39,46,47] in recent work it has been shown that Fe-Ni alloy nanoparticles can be exsolved from Fe- and Ni-containing perovskite oxides, including $(La_{0.7}Sr_{0.3})(Cr_{0.85}Ni_{0.1125}Fe_{0.0375})O_{3-x}$, $La_{0.6}Sr_{0.4}Fe_{0.8}Ni_{0.2}O_{3-\delta}$, and $Sr_2FeMo_{0.65}Ni_{0.35}O_{6-\delta}$.[33,43,48] Thalinger et.al. observed (Fe,Ni) alloy particles

at the $La_{0.6}Sr_{0.4}FeO_{3-\delta}$ (LSF) oxide surface after reduction in H_2 at 600°C with Ni-infiltrated LSF.[49] Other alloy nanoparticles such as Cu-Ni have also been formed on rutile oxides.[50] One important question regarding these oxides containing multiple reducible cations is what determines the composition of the alloy nanoparticles. There are two previous reports where the alloy composition was measured. In one case, the XRD-measured alloy composition was $Fe_{0.64}Ni_{0.36}$ for an $La_{0.6}Sr_{0.4}Fe_{0.8}Ni_{0.2}O_{3-\delta}$ oxide.[48] In another case it was assumed that the particles were $FeNi_3$ for a $Sr_2FeMo_{1-x}Ni_xO_{6-\delta}$ (x = 0.25–0.35) oxide, although the measured lattice parameter indicated an alloy with ~40% Fe.[41,43] In the present case, the alloy contains ~49%–55% Fe; this is much more Ni rich than the Ni/Fe ratio in the STFN.

The above literature review shows that there are few accurate experimental measurements of exsolved nanoparticle composition, yet the composition is likely important in determining their electrochemical activity.[51] In general, it is not clear which cations will exsolve from an oxide anode, and under which conditions. For example, in the present result, it is not clear why metallic Fe is present in the nanoparticles formed on STFN under SOFC anode conditions, whereas Fe in the Ni-free analog (STF) is stable against reduction under the same conditions. The same question is probably relevant to other reports on Fe-Ni-containing oxides discussed above, although comparison data regarding the stability of the corresponding Ni-free oxides was not provided in those reports.[43,48] Separate measurements on stoichiometric STFN, not shown here, yield similar exsolution results, indicating that A-site deficiency is not the main driver of Fe exsolution.

A thermodynamic model is proposed here that predicts nanoparticle composition. For high enough effective oxygen partial pressure $p_{O_2}^{Fuel}$ in the fuel neither cation exsolves, whereas for low enough $p_{O_2}^{Fuel}$, both cations completely exsolve, likely resulting in decomposition of the perovskite. The following analysis applies in general to a middle range of $p_{O_2}^{Fuel}$ where one cation (Ni for the present STFN oxide) is readily reduced, whereas the other (Fe in the present case) remains oxidized in the absence of the more reducible cation. The overall exsolution reaction can be written as:

$$Sr_{0.95}(Ti_{0.3}Fe_{0.63}Ni_{0.07})O_{3-\delta} \rightarrow Sr_{0.95}\left(Ti_{0.3}Fe_{0.63-y}\right)O_{3-\delta-\frac{3y}{2}-0.07} + yFe_{(in\ Fe\text{-}Ni)} + 0.07Ni_{in\ Fe-Ni} + \left(\frac{3y}{4} + 0.035\right)O_2\ , \quad \text{(Equation 1)}$$

where y is the amount of Fe exsolved. This reaction can be split into separate Ni and Fe reduction reactions:

$$Sr_{0.95}(Ti_{0.3}Fe_{0.63}Ni_{0.07})O_{3-\delta} \rightarrow Sr_{0.95}(Ti_{0.3}Fe_{0.63})O_{3-\delta-0.07} + 0.07Ni_{in\ Fe-Ni} + (0.035)O_2. \quad \text{(Equation 2)}$$

and

$$Sr_{0.95}(Ti_{0.3}Fe_{0.63})O_{3-\delta-0.07} \rightarrow Sr_{0.95}\left(Ti_{0.3}Fe_{0.63-y}\right)O_{3-\delta-\frac{3y}{2}-0.07} + yFe_{(in\ Fe\text{-}Ni)} + \left(\frac{3y}{4}\right)O_2. \quad \text{(Equation 3)}$$

The oxide stoichiometry in Equation 1 is taken as Fe_2O_3 since Fe has been shown to be present in the Fe^{+3} oxidation state in STF under these conditions.[52] These equations are written without any oxide second phases (e.g., SrO), despite the fact that the oxide is becoming increasingly B-site deficient during exsolution; it is assumed that the amount exsolved is small enough to retain a perovskite-structure

oxide, as needed for good anode performance. For these conditions, the more reducible cation is completely exsolved, as observed in the present case where no Ni is detected in STFN after extended exposure to fuel (Table 1). That is, it is known that Equation 2 proceeds to completion. It remains to determine the amount of Fe exsolved in Equation 3, and hence the composition of the nanoparticles. The equilibrium constant for Equation 3 is given by

$$K = \frac{a_{STF-y} a_{Fe}^{y} \left(p_{O2}^{Fuel}\right)^{3y/4}}{a_{STF}}, \qquad \text{(Equation 4)}$$

where a_{STF} is the activity of STF before Fe exsolution, and a_{STF-y} is the activity of STF after Fe exsolution. Using this in the reaction equilibrium condition $\Delta G^0 = -RTlnK$ yields

$$a_{Fe}^{y} = \left(p_{O2}^{Fuel}\right)^{-3y/4} \frac{a_{STF}}{a_{STF-y}} \exp\left(-\frac{\Delta G^0}{RT}\right). \qquad \text{(Equation 5)}$$

ΔG^0 is the standard free energy of reaction 3. The activity ratio in Equation 5 accounts for the change in activity due to Fe exsolution. Since these quantities are not known, we have used a separate measurement to evaluate Equation 5. Note that the STF compositions in Equation 3 are very similar to that of the standard stoichiometric STF composition discussed above, $SrTi_{0.3}Fe_{0.7}O_{3-\delta}$. For this material, we used TG to measure the equilibrium oxygen partial pressure p_{O2}^{Red} below which Fe is reduced, via the reaction

$$Sr(Ti_{0.3}Fe_{0.7})O_{3-\delta} \rightarrow Sr(Ti_{0.3}Fe_{0.7-x})O_{3-\delta-\frac{3y}{2}} + yFe + \left(\frac{3y}{4}\right)O_2. \qquad \text{(Equation 6)}$$

Since there is no exsolved Ni in this case, any metallic Fe nanoparticles formed are pure, and $a_{Fe(pure\ Fe)} = 1$ such that

$$a_{Fe}^{y} = 1 = \left(p_{O2}^{Red}\right)^{-3y/4} \frac{a_{STF}}{a_{STF-y}} \exp\left(-\frac{\Delta G^0}{RT}\right). \qquad \text{(Equation 7)}$$

Because the STF compositions in this reaction are almost identical to those in Equation 3, the activity ratio and ΔG^0 should be approximately the same, and we can substitute Equation 7 into Equation 5, yielding

$$a_{Fe(in\ Fe-Ni)} \cong \left(\frac{p_{O2}^{Red}}{p_{O2}^{Fuel}}\right)^{3/4}. \qquad \text{(Equation 8)}$$

Assuming that the Fe_xNi_{1-x} alloy can be approximated as a regular solution, where $a_{Fe} = x\ exp\left[\frac{\Omega(1-x)^2}{RT}\right]$ with a binary alloy interaction parameter $\Omega_{Fe-Ni} = -8$ kJ mol^{-1},[53] this yields for the alloy composition x:

$$x\ exp\left[\frac{\Omega(1-x)^2}{RT}\right] = \left(\frac{p_{O2}^{Red}}{p_{O2}^{Fuel}}\right)^{3/4}. \qquad \text{(Equation 9)}$$

This predicts that metallic Fe is present in exsolved nanoparticles for $p_{O2}^{Fuel} > p_{O2}^{Red}$, with equilibrium composition x that varies with p_{O2}^{Fuel}. That is, Fe is reduced from STFN under conditions where Fe in STF is stable. Physically, this occurs because both the entropy of mixing and the negative value of Ω_{Fe-Ni} make it thermodynamically favorable to form the Fe-Ni alloy under conditions where pure Fe does not form. Equation 9 predicts that $\frac{p_{O2}^{Red}}{p_{O2}^{Fuel}}$ should be ~0.30 to form nanoparticles with the observed composition $x \sim 0.5$ (Table 1). Given the value $p_{O2}^{Fuel} = 5.9 \times 10^{-20}$ atm in the fuel used for the STFN reduction, this suggests that $p_{O2}^{Red} = 1.8 \times 10^{-20}$ atm.

This agrees well with the TG observations that STF at 850°C decomposed for 0.79×10^{-20} atm (corresponding to a 75% H_2/3% H_2O mixture) but was stable for 2.6×10^{-20} atm. That is, p_{O2}^{Fuel} was between 0.79×10^{-20} atm and 2.6×10^{-20} atm. Our preliminary results for STFN reduction at a different p_{O2}^{Fuel} are also consistent with Equation 9, which predicts that the Fe content x should decrease as p_{O2}^{Fuel} is increased. For example, for p_{O2}^{Fuel} increased to 4.0×10^{-20} atm at 850°C (10% H_2/3% H_2O/87%Ar), the composition predicted for the alloy is $Fe_{0.3}Ni_{0.7}$, in reasonable agreement with the composition obtained from XRD measurements: $Fe_{0.28}Ni_{0.72}$. The different Fe-Ni alloy compositions formed in prior reports[43,48] probably resulted because of the different oxides involved, or because of different p_{O2}^{Fuel} values.

Note that Equations 8 and 9 can be applied to any cation in an oxide undergoing exsolution of a more reducible cation dopant. A more general form of Equation 8 is

$$a_{Cat} \approx \left(\frac{p_{O2}^{Red}}{p_{O2}^{Fuel}}\right)^{m/4}, \qquad \text{(Equation 10)}$$

where a_{Cat} is the activity of the cation in the nanoparticles, m is the oxidation state of the cation in the oxide, p_{O2}^{Red} is the critical oxygen partial pressure for reduction of the cation in the undoped oxide, and p_{O2}^{Fuel} is the effective fuel oxygen partial pressure during exsolution. Note that Equation 10 is consistent with the observation that cations forming very stable oxides, such as Ti in the present STFN oxide, do not appear in exsolved nanoparticles. For such cations, p_{O2}^{Red} is very low compared with typical p_{O2}^{Fuel} values in SOFC fuels, such that Equation 10 predicts a very low a_{Cat}, and hence low cation mole fraction x_{Cat}. In order to use Equation 10 to predict nanoparticle composition for any exsolution oxide material, one needs to measure the value p_{O2}^{Red} for the oxide without the reducible cation (as we have done here for STF), and to have a thermodynamic model for the metal alloy system in order to determine the composition from a_{Cat}.

The above results show that the oxide loses Fe and Ni B-site cations during exsolution. Although STFN is initially 5% A-site deficient, the loss of most or all the Ni (5%–7% of the B-site cations, accounting for error in TEM-EDS measurements) and an approximately equal amount of Fe corresponds to 10%–14% of the B-site cations, leaving an overall 5%–9% B-site deficient composition, e.g., $Sr(Ti_{0.32}Fe_{0.59})O_{3-\delta}$. (Alternatively, the same composition can be written as A-site-rich $Sr_{1.1}(Ti_{0.35}Fe_{0.65})O_{3-\delta}$.) Although the TEM-EDS data from the oxide phase (Table 1) suggests that the perovskite is closer to stoichiometric, this discrepancy could be due to experimental error and possible spatial composition variations. Any Sr excess could be accommodated by perovskite non-stoichiometry or production of additional Sr-rich phases, or a combination of both. We suggest the following interpretation: any Sr excess of the oxide phase is partly accommodated by perovskite non-stoichiometry and partly by the formation of a more Sr-rich perovskite-related phase, e.g., layered nickelate-structure $Sr_2(Ti,Fe)O_4$. This could explain the oxide contrast observed in the TEM images in Figures 4A and 4B after exsolution. In particular, the lattice-fringe striations may indicate partial conversion of the perovskite to a layered phase similar to those reported by Canales-Vázquez et al for La-Sr titanates.[42] It is also possible that second-phase SrO forms, but is not detected because of its small amount or due to conversion to amorphous SrO, $SrCO_3$, or $Sr(OH)_2$ during air exposure prior to measurement.

Electrochemical Performance

The much better electrochemical performance of STFN anodes compared with STF is presumably explained by the presence of exsolved nanoparticles on oxide anode surfaces, analogous to previous reports for various oxide exsolution anodes.[8,27] The positive effect of Ni-Fe alloy nanoparticles also agrees with prior reports where this alloy has been shown to be an effective anode electrocatalyst.[25,51,54] It is also possible that changes in the oxide composition and structure upon exsolution play a role in the electrochemical characteristics; however, it is unclear whether such changes have a beneficial or detrimental effect. Preliminary results on an alternate STFN composition with no A-site deficiency showed similar exsolution but much worse electrochemical performance than the A-site-deficient STFN. This may be the result of the greater B-site deficiency that results after exsolution from stoichiometric STFN, expected to yield a substantial phase change that impairs electrochemical performance.

One unique feature of the present results is that a direct comparison with the analogous Ni-free and nanoparticle-free oxide (STF) is provided for a range of operating temperatures and hydrogen partial pressures. Although the STF and STFN cells showed similar performance at 850°C and p_{H_2} = 0.97 atm, as temperature and p_{H_2} decreased the STF cell performance degraded much more rapidly. That is, STFN cell power density was much higher and polarization resistance much lower at reduced temperature and p_{H_2} (Figure 7). The STF cell results can be understood based on a recent study of these anodes, where a limiting current behavior was observed in the *j-V* curves; the limiting current decreased rapidly with decreasing p_{H_2}, explained by a rate-limiting H_2 dissociative adsorption process.[21] Although the cathodes in the present STF cells are different to those described by Zhu et al.,[21] the cells exhibited similar *j-V* behavior, including an anomalous increase in *j* at low *V* that was explained by a change in oxide stoichiometry. In contrast, the STFN-anode cells showed a generally positive curvature in the *j-V* curves, with no indication of limiting current except at low temperatures and p_{H_2}. Furthermore, $R_{P,A}$ versus pressure follows a power law dependence, $\sim p_{H2}^{-0.25}$, suggesting a charge transfer process was the rate-limiting step for STFN. The STF results show a stronger p_{H_2} dependence that is consistent with an adsorption rate limitation.[21] These results can presumably be explained by the presence of Fe-Ni nanoparticles on the STFN-anode surfaces that promote H_2 dissociation, with adsorbed atomic hydrogen spilling over onto the oxide surface for subsequent electrochemical oxidation, similar to composite anodes such as Ni-YSZ.[44,55] The same argument was used to explain the effects of exsolved Ru nanoparticles in a (La,Sr)(Cr,Ru)O_3 anode cell.[21]

Conclusions

The substitution of Ni for Fe in $SrTi_{0.3}Fe_{0.7}O_{3-\delta}$ (STF) perovskite oxide anodes, to form compounds with A-site-deficient composition $Sr_{0.95}(Ti_{0.3}Fe_{0.63}Ni_{0.07})O_{3-\delta}$ (STFN), was studied. Key findings and conclusions are as follows:

(1) Upon exposure to reducing fuel conditions ($pO_2 = 5.9 \times 10^{-20}$ atm, 850°C), Ni and Fe exsolve from STFN resulting in the formation of metallic $Ni_{1-x}Fe_x$ alloy nanoparticles with diameters of 40–70 nm and composition $x \sim 0.50$. This alloy composition estimate is verified using three different methods, compared with recent reports of alloy exsolution from $La_{0.6}Sr_{0.4}Fe_{0.8}Ni_{0.2}O_{3-\delta}$[48] and $Sr_2FeMo_{1-x}Ni_xO_{6-\delta}$ (x = 0.25–0.35)[43] anodes, where the nanoparticle composition was approximate.

(2) The exsolution of Fe from STFN into the Ni-Fe alloy, at a pO_2 where Fe does not exsolve from STF, is explained based on the thermodynamic properties of mixing of the metallic alloy. The calculation indicates that the Fe-Ni alloy composition will become more Ni rich as the effective oxygen partial pressure in the fuel increases. Thus, if these anodes were used in an SOFC stack, where effective pO_2 varies considerably between the fuel inlet and outlet, the nanoparticle composition will vary substantially with position. If the activity of the nanoparticles improves with increasing Ni content, this could provide a means for helping to maintain uniform performance at high fuel utilization.

(3) It is shown that gravimetric measurements can be used to observe the oxygen loss associated with exsolution and reduction of Ni-Fe. In this way, the rate of the exsolution process is determined and, with some assumptions, the alloy composition is estimated.

(4) Comparison of STFN-anode and STF-anode cell electrochemical data show important performance enhancements due to the Ni substitution, particularly for low pH_2 and temperatures <800°C. The results suggest that the Ni-Fe nanoparticles act to enhance hydrogen dissociative adsorption, a key fuel oxidation rate-limiting step found in a prior study of STF anodes to limit performance at low pH_2 and temperature.

(5) Cells with the A-site deficient $Sr_{0.95}(Ti_{0.3}Fe_{0.63}Ni_{0.07})O_{3-\delta}$ (STFN) anode yield relatively high maximum power density, e.g., 0.95 W cm^{-2} at 800°C in humidified hydrogen and air, with low anode polarization resistance of 0.081 $\Omega \cdot cm^2$. This performance is competitive with the widely used Ni-YSZ anodes, such that it will be worthwhile to explore potential advantages of these anodes in terms of redox cycling, coking, and impurity tolerance. Also, it has been suggested that Ni-Fe alloys are resistant to coking and sulfur poisoning.[33,43,56] It will also be interesting to explore whether these anodes can be integrated into thin-electrolyte SOFCs, in order to further improve cell performance.

(6) The electrochemical performance enhancements result from relatively large (~50 nm) nanoparticles that appear to be reasonably stable in initial life tests, but more long-term stability tests are needed.

EXPERIMENTAL PROCEDURES

Materials Preparation

The solid-state reaction method was used to prepare $SrTi_{0.3}Fe_{0.7}O_{3-\delta}$ (STF) and $Sr_{0.95}(Ti_{0.3}Fe_{0.63}Ni_{0.07})O_{3-\delta}$ (STFN). An A-site deficient composition was chosen since prior work has shown that A-site deficiency promotes B-site metal exsolution and also results in a more stoichiometric perovskite after exsolving B-site transition metals.[39] The starting materials were $SrCO_3$, TiO_2, Fe_2O_3, and $Ni(NO_3)_2 \cdot 6H_2O$ (Sigma-Aldrich), as reported previously.[21] The calcinations of the precursor were conducted in air at 1,200°C for 10 hr. The derived powders were ball-milled in ethanol for 4 days and then dried. LSGM electrolyte pellets (~300 μm in thickness, ~15.5 mm in diameter) with $La_{0.4}Ce_{0.6}O_{2-\delta}$ (LDC) barrier layer (~3 μm in thickness) were prepared as described elsewhere.[21,24,36]

Cell Fabrication

Single cells with STF or STFN anodes and LSCF-GDC/LSCF cathodes (electrode areas of 0.5 cm^2) were prepared on the LSGM/LDC electrolytes as follows. STF, STFN, $La_{0.6}Sr_{0.4}Co_{0.2}Fe_{0.8}O_{3-\delta}$ (LSCF, Praxair), and LSCF-$Gd_{0.1}Ce_{0.9}O_{1.95}$ (GDC, Praxair; LSCF/GDC = 1:1, wt %) electrode inks were prepared by mixing the corresponding electrode powder and binder (V-737, Heraeus) on a three-roll mill with weight ratio of 1:1.5. STF and STFN-anode inks were screen printed on the

LDC-coated LSGM pellets and fired at 1,150°C for 3 hr in air. The LSCF-GDC cathode layer and LSCF current collector layers were screen printed on the LSGM electrolytes and fired at 1,075°C for 2 hr. Gold ink (Heraeus C5756) was screen printed as a 1-mm square mesh pattern on the electrodes and fired at 900°C for 1 hr to form the current collectors.

Structure and Microstructure Characterization

Structural characterization was carried out on both the as-prepared and reduced anode powders. The reduction procedure was as follows: heating up to 850°C under Ar flow, then switching the gas composition to 30% H_2/67% Ar/3% H_2O, and maintaining at 850°C for 4 hr. This is identical to the procedure used to pre-reduce the cells (see below), thus ensuring that the powders were in the same state as the anodes at the onset of electrochemical testing. Although it was found that the TG-measured mass was not quite equilibrated after 4 hr, the mass loss was estimated to be within a few percent of equilibrium. The samples were then quenched to freeze-in their structure for *ex situ* analysis. This procedure was performed inside a TG setup described in detail elsewhere.[57] The powder mass loss was measured in the thermobalance during the above procedure, with measured mass change accuracy within ± 10 μg for ~0.6-g powder samples of STF and STFN, therefore exposed to the reducing atmosphere. The gas mixture was measured with a ZrO_2-based electrochemical O_2 sensor to assure the same effective oxygen partial pressure, 5.9×10^{-20} atm, as it was present during the cell test at open circuit, V_{OC} = 1.054 V at 850°C. The mass was related to the oxygen content and Fe oxidation state by taking into account the formation of a plateau in the isotherms of mass versus the oxygen partial pressure (pO_2) for the STF. Isotherms are taken between 650°C and 900°C and pO_2 range between 10^{-25} and 1 bar by using O_2/Ar and H_2/H_2O/Ar mixtures. A plateau in oxygen content was observed from $pO_2 \sim 10^{-5}$ to 10^{-16} atm at 850°C and 10^{-5} to 10^{-20} atm at 650°C,[52] which was assumed to be where all Fe cations are in the Fe^{+3} state,[58] corresponding to $3 - \delta = 2.65$. After the TG measurement, the quenched powders were removed and characterized by powder XRD and electron transmission microscopy (TEM). The XRD was performed using a PANalytical Empyrean equipment with Cu-Kα radiation, monochromator, and Pixel3D detector. TEM studies were performed under both Philips CM 200 (LaB6) and TECNAI F-20 transmission electron microscopes equipped with an Ultra Twin objective lens, which operate at 200 kV. The microscopes are also equipped with a CCD camera and respective EDAX detectors, useful for analysis of local chemical composition.

Electrochemical Characterization

The single cells were sealed on top of alumina tubes using silver (DAD-87, Shanghai Research Institute of Synthetic Resins). In all cases, prior to testing the cells were heated at a rate of 2°C min^{-1} up to 850°C with anode exposed in Ar, and maintained at that temperature for 4 hr after switching anode gas to room temperature humidified H_2. This pre-reduction at high temperature resulted in the growth of relatively large and stable exsolved nanoparticles, such that the anode performance was found to be quite stable in subsequent testing at lower temperatures, as shown in Figure S1. This is different from many prior exsolution anodes where the performance varies during testing due to nanoparticle evolution.[8,27] During electrochemical testing, the anodes were fed with room temperature humidified H_2/Ar (~3% H_2O/H_2/Ar, 100 mL·min^{-1}), and the cathodes were exposed to stagnant ambient air. The EIS and current-voltage curves under different temperatures and anode H_2 partial pressures were tested with Zahner IM6 Electrochemical Workstations; EIS tests were conducted in the frequency range from 0.1 Hz to 1 MHz with

potential amplitude of 20 mV. After testing, the cell microstructures were characterized using scanning electron microscopy under a Hitachi SU8030.

SUPPLEMENTAL INFORMATION

Supplemental Information includes one figure and can be found with this article online at https://doi.org/10.1016/j.joule.2018.02.006.

ACKNOWLEDGMENTS

The authors at Northwestern University gratefully acknowledge financial support by the US Department of Energy (grant #DE-SC0016965), those at Centro Atómico acknowledge AGNPCyT (PICT 2013-1032), CONICET (11220150100565CO), and Universidad Nacional de Cuyo, and those at Tsinghua University acknowledge Ministry of Science and Technology of China (2017YFB0601901 and 2017YFB0601903) and Tsinghua University Initiative Scientific Research Program (2015THZ0). T.Z. gratefully acknowledges the scholarship from the State Scholarship Fund of China Scholarship Council (201406430041). The authors also acknowledge the assistance of the Electron Probe Instrumentation Center (EPIC) at the NUANCE Center, Northwestern University, which has received support from the Soft and Hybrid Nanotechnology Experimental (SHyNE) Resource (NSF NNCI-1542205); the MRSEC program (NSF DMR-1121262) at the Materials Research Center; the International Institute for Nanotechnology (IIN); the Keck Foundation; and the State of Illinois, through the IIN.

AUTHOR CONTRIBUTIONS

S.A.B. conceived and supervised the project. T.Z. synthesized the materials, fabricated the cells, and performed electrochemical and scanning electron microscopy tests. H.E.T. and L.V.M. conducted the TG, XRD, and TEM tests. S.A.B. and L.V.M. developed the metal alloy exsolution theory. All authors (T.Z., H.E.T., L.V.M., M.H., and S.A.B.) wrote the manuscript.

DECLARATION OF INTERESTS

The authors declare no competing interests.

Received: June 26, 2017
Revised: November 13, 2017
Accepted: December 10, 2017
Published: February 28, 2018

REFERENCES

1. Atkinson, A., Barnett, S.A., Gorte, R.J., Irvine, J.T.S., McEvoy, A.J., Mogensen, M.B., Singhal, S., and Vohs, J. (2004). Advanced anodes for high temperature fuel cells. Nat. Mater. *3*, 17–27.

2. McIntosh, S., and Gorte, R.J. (2004). Direct hydrocarbon solid oxide fuel cells. Chem. Rev. *104*, 4845–4865.

3. Tao, S., and Irvine, J.T.S. (2004). Discovery and characterization of novel oxide anodes for solid oxide fuel cells. Chem. Rec. *4*, 83–95.

4. Menzler, N.H., Tietz, F., Uhlenbruck, S., Buchkremer, H.P., and Stover, D. (2010). Materials and manufacturing technologies for solid oxide fuel cells. J. Mater. Sci. *45*, 3109–3135.

5. Sarantaridis, D., Chater, R.J., and Atkinson, A. (2008). Changes in physical and mechanical properties of SOFC Ni-YSZ composites caused by redox cycling. J. Electrochem. Soc. *155*, B467–B472.

6. Botti, J.J. (2003). The revolution through evolution: delphi solid oxide fuel cell for APU and hydrogen reformation. In SOFC VIII, S.C. Singhal and J. Mizusaki, eds. (Electrochemical Society), pp. 16–30.

7. Haag, J.M., Madsen, B.D., Barnett, S.A., and Poeppelmeier, K.R. (2008). Application of $LaSr_2Fe_2CrO_9$ in solid oxide fuel cell anodes. Electrochem. Solid-State Lett. *11*, B51–B53.

8. Madsen, B.D., Kobsiriphat, W., Wang, Y., Marks, L.D., and Barnett, S.A. (2007). Nucleation of nanometer-scale electrocatalyst particles in solid oxide fuel cell anodes. J. Power Sourc. *166*, 64–67.

9. Madsen, B.D., and Barnett, S.A. (2007). $La_{0.8}Sr_{0.2}Cr_{0.98}V_{0.02}O_{3-\delta}Ce_{0.9}Gd_{0.1}O_{1.95}$-Ni anodes for solid oxide fuel cells. J. Electrochem. Soc. *154*, B501–B507.

10. Ji, Y., Huang, Y.-H., Ying, J.-R., and Goodenough, J.B. (2007). Electrochemical performance of La-doped Sr2MgMoO6-[delta] in natural gas. Electrochem. Commun. *9*, 1881–1885.

11. Goodenough, J.B., and Huang, Y.-H. (2007). Alternative anode materials for solid oxide fuel cells. J. Power Sourc. *173*, 1–10.

12. Huang, Y.-H., Dass, R.I., Xing, Z.-L., and Goodenough, J.B. (2006). Double perovskites as anode materials for solid-oxide fuel cells. Science *312*, 254–257.

13. Ahn, K., Jung, S., Vohs, J.M., and Gorte, R.J. (2007). A support layer for solid oxide fuel cells. Ceramics Int. *33*, 1065–1070.

14. Gross, M.D., Vohs, J.M., and Gorte, R.J. (2007). A strategy for achieving high performance with SOFC ceramic anodes. Electrochem. Solid-State Lett. *10*, B65–B69.

15. Marina, O.A., and Pederson, L.R. (2002). Novel ceramic anodes for SOFCs tolerant to oxygen, carbon and sulfur. In The Fifth European Solid Oxide Fuel Cell Forum; July 1-5, 2002, J. Huijismans, ed. (European Fuel Cell Forum), pp. 481–489.

16. Marina, O.A., Canfield, N.L., and Stevenson, J.W. (2002). Thermal, electrical, and electrocatalytical properties of lanthanum-doped strontium titanate. Solid State Ionics *149*, 21–28.

17. Fu, Q., Tietz, F., Sebold, D., Tao, S., and Irvine, J.T.S. (2007). An efficient ceramic-based anode for solid oxide fuel cells. J. Power Sourc. *171*, 663–669.

18. Tao, S., and Irvine, J.T.S. (2004). Synthesis and characterization of $(La_{0.75}Sr_{0.25})Cr_{0.5}Mn_{0.5}O_{3-d}$, a redox-stable, efficient perovskite anode of SOFCs. J. Electrochem. Soc. *151*, A252–A259.

19. McIntosh, S., Vohs, J.M., and Gorte, R.J. (2003). Effect of precious-metal dopants on SOFC anodes for direct utilization of hydrocarbons. Electrochem. Solid-State Lett. *6*, A240.

20. Tao, S., and Irvine, J.T.S. (2003). A redox-stable efficient anode for solid-oxide fuel cells. Nat. Mater. *2*, 320–323.

21. Zhu, T., Fowler, D.E., Poeppelmeier, K.R., Han, M., and Barnett, S.A. (2016). Hydrogen oxidation mechanisms on perovskite solid oxide fuel cell anodes. J. Electrochem. Soc. *163*, F952–F961.

22. Fowler, D.E., Messner, A.C., Miller, E.C., Slone, B.W., Barnett, S.A., and Poeppelmeier, K.R. (2015). Decreasing the polarization resistance of $(La,Sr)CrO_{3-\delta}$ solid oxide fuel cell anodes by combined Fe and Ru substitution. Chem. Mater. *27*, 3683–3693.

23. Xiao, G., and Chen, F. (2014). Redox stable anodes for solid oxide fuel cells. Front. Energy Res. *2*, https://doi.org/10.3389/fenrg.2014.00018.

24. Cho, S., Fowler, D.E., Miller, E.C., Cronin, J.S., Poeppelmeier, K.R., and Barnett, S.A. (2013). Fe-substituted $SrTiO_{3-\delta}$-$Ce_{0.9}Gd_{0.1}O_2$ composite anodes for solid oxide fuel cells. Energy Environ. Sci. *6*, 1850.

25. Tucker, M.C. (2010). Progress in metal-supported solid oxide fuel cells: a review. J. Power Sourc. *195*, 4570–4582.

26. Nielsen, J., Klemensø, T., and Blennow, P. (2012). Detailed impedance characterization of a well performing and durable Ni:CGO infiltrated cermet anode for metal-supported solid oxide fuel cells. J. Power Sourc. *219*, 305–316.

27. Kobsiriphat, W., Madsen, B.D., Wang, Y., Marks, L.D., and Barnett, S.A. (2009). $La_{0.8}Sr_{0.2}Cr_{1-x}Ru_xO_{3-\delta}$-$Gd_{0.1}Ce_{0.9}O_{1.95}$ solid oxide fuel cell anodes: Ru precipitation and electrochemical performance. Solid State Ionics *180*, 257–264.

28. Kobsiriphat, W., Madsen, B.D., Wang, Y., Shah, M., Marks, L.D., and Barnett, S.A. (2010). Nickel- and ruthenium-doped lanthanum chromite anodes: effects of nanoscale metal precipitation on solid oxide fuel cell performance. J. Electrochem. Soc. *157*, B279.

29. Bierschenk, D.M., Potter-Nelson, E., Hoel, C., Liao, Y., Marks, L., Poeppelmeier, K.R., and Barnett, S.A. (2011). Pd-substituted $(La,Sr)CrO_{3-\delta}$-$Ce_{0.9}Gd_{0.1}O_{2-\delta}$ solid oxide fuel cell anodes exhibiting regenerative behavior. J. Power Sourc. *196*, 3089–3094.

30. Neagu, D., Oh, T.S., Miller, D.N., Menard, H., Bukhari, S.M., Gamble, S.R., Gorte, R.J., Vohs, J.M., and Irvine, J.T. (2015). Nano-socketed nickel particles with enhanced coking resistance grown in situ by redox exsolution. Nat. Commun. *6*, 8120.

31. Madsen, B.D., Kobsiriphat, W., Wang, Y., Marks, L.D., and Barnett, S.A. (2007). SOFC anode performance enhancement through precipitation of nanoscale catalysts. ECS Trans. *7*, 1339–1348.

32. Yang, C., Yang, Z., Jin, C., Xiao, G., Chen, F., and Han, M. (2012). Sulfur-tolerant redox-reversible anode material for direct hydrocarbon solid oxide fuel cells. Adv. Mater. *24*, 1439–1443.

33. Sun, Y.F., Li, J.H., Cui, L., Hua, B., Cui, S.H., Li, J., and Luo, J.L. (2015). A-site-deficiency facilitated in situ growth of bimetallic Ni-Fe nano-alloys: a novel coking-tolerant fuel cell anode catalyst. Nanoscale *7*, 11173–11181.

34. Luo, T., Liu, X., Meng, X., Wu, H., Wang, S., and Zhan, Z. (2015). In situ formation of $LaNi_{0.6}Fe_{0.4}O_{3-\delta}$-carbon nanotube hybrids as anodes for direct-methane solid oxide fuel cells. J. Power Sourc. *299*, 472–479.

35. Yang, Z., Chen, Y., Xu, N., Niu, Y., Han, M., and Chen, F. (2015). Stability investigation for symmetric solid oxide fuel cell with $La_{0.4}Sr_{0.6}Co_{0.2}Fe_{0.7}Nb_{0.1}O_{3-\delta}$ electrode. J. Electrochem. Soc. *162*, F718–F721.

36. Zhu, T., Yang, Z., and Han, M. (2015). Performance evaluation of solid oxide fuel cell with in-situ methane reforming. Fuel *161*, 168–173.

37. Myung, J.H., Neagu, D., Miller, D.N., and Irvine, J.T. (2016). Switching on electrocatalytic activity in solid oxide cells. Nature *537*, 528–531.

38. Ye, L., Zhang, M., Huang, P., Guo, G., Hong, M., Li, C., Irvine, J.T., and Xie, K. (2017). Enhancing CO_2 electrolysis through synergistic control of non-stoichiometry and doping to tune cathode surface structures. Nat. Commun. *8*, 14785.

39. Neagu, D., Tsekouras, G., Miller, D.N., Menard, H., and Irvine, J.T. (2013). In situ growth of nanoparticles through control of non-stoichiometry. Nat. Chem. *5*, 916–923.

40. Oh, T.S., Rahani, E.K., Neagu, D., Irvine, J.T., Shenoy, V.B., Gorte, R.J., and Vohs, J.M. (2015). Evidence and model for strain-driven release of metal nanocatalysts from perovskites during exsolution. J. Phys. Chem. Lett. *6*, 5106–5110.

41. Hayase, M., Shiga, M., and Nakamura, Y. (1973). Spontaneous volume magnetostriction and lattice constant of face-centered cubic Fe-Ni and Bi-Cu alloys. J. Phys. Soc. Jpn. *34*, 925–931.

42. Canales-Vázquez, J., Smith, M.J., Irvine, J.T.S., and Zhou, W. (2005). Studies on the reorganization of extended defects with increasing n in the perovskite-based $La_4Sr_{n-4}TinO_{3n+2}$ series. Adv. Funct. Mater. *15*, 1000–1008.

43. Du, Z., Zhao, H., Yi, S., Xia, Q., Gong, Y., Zhang, Y., Cheng, X., Li, Y., Gu, L., and Swierczek, K. (2016). High-performance anode material $Sr_2FeMo_{0.65}Ni_{0.35}O_{6-\delta}$ with in situ exsolved nanoparticle catalyst. ACS Nano *10*, 8660–8669.

44. Bessler, W.G. (2005). A new computational approach for SOFC impedance from detailed electrochemical reaction-diffusion models. Solid State Ionics *176*, 997–1011.

45. Kennouche, D., Chen-Wiegart, Y.c.K., Cronin, J.S., Wang, J., and Barnett, S.A. (2013). Three-dimensional microstructural evolution of Ni-Yttria-stabilized zirconia solid oxide fuel cell anodes at elevated temperatures. J. Electrochem. Soc. *160*, F1293–F1304.

46. Xiao, G., Wang, S., Lin, Y., Zhang, Y., An, K., and Chen, F. (2014). Releasing metal catalysts via phase transition: $(NiO)_{0.05}$-$(SrTi_{0.8}Nb_{0.2}O_3)_{0.95}$ as a redox stable anode material for solid oxide fuel cells. ACS Appl. Mater. Interfaces *6*, 19990–19996.

47. Sun, Y.-F., Li, J.-H., Wang, M.-N., Hua, B., Li, J., and Luo, J.-L. (2015). A-site deficient chromite perovskite with in situ exsolution of nano-Fe: a promising bi-functional catalyst bridging the growth of CNTs and SOFCs. J. Mater. Chem. A *3*, 14625–14630.

48. Liu, S., Liu, Q., and Luo, J.-L. (2016). Highly stable and efficient catalyst with in situ exsolved Fe-Ni alloy nanospheres socketed on an oxygen deficient perovskite for direct CO_2 electrolysis. ACS Catal. *6*, 6219–6228.

49. Thalinger, R., Gocyla, M., Heggen, M., Klotzer, B., and Penner, S. (2015). Exsolution of Fe and SrO nanorods and nanoparticles from lanthanum strontium ferrite $La_{0.6}Sr_{0.4}FeO_{3-\delta}$ materials by hydrogen reduction. J. Phys. Chem. C Nanomater. Interfaces *119*, 22050–22056.

50. Wei, H., Xie, K., Zhang, J., Zhang, Y., Wang, Y., Qin, Y., Cui, J., Yan, J., and Wu, Y. (2014). In situ growth of Ni(x)Cu(1-x) alloy nanocatalysts on redox-reversible rutile (Nb,Ti)O(4) towards high-temperature carbon dioxide electrolysis. Sci. Rep. *4*, 5156.

51. Lu, X.C., Zhu, J.H., and Bi, Z.H. (2009). Fe alloying effect on the performance of the Ni anode in hydrogen fuel. Solid State Ionics *180*, 265–270.

52. Nenning, A., Volgger, L., Miller, E., Mogni, L.V., Barnett, S., and Fleig, J. (2017). The

electrochemical properties of Sr(Ti,Fe)$O_{3-\delta}$ for anodes in solid oxide fuel cells. J. Electrochem. Soc. *164*, F364–F371.

53. Takeuchi, A., and Inoue, A. (2000). Calculations of mixing enthalpy and mismatch entropy for ternary amorphous alloys. Mater. Trans. JIM *41*, 1372–1378.

54. Ju, Y.-W., Eto, H., Inagaki, T., Ida, S., and Ishihara, T. (2010). Preparation of Ni-Fe bimetallic porous anode support for solid oxide fuel cells using $LaGaO_3$ based electrolyte film with high power density. J. Power Sourc. *195*, 6294–6300.

55. Zhu, H., Kee, R.J., Janardhanan, V.M., Deutschmann, O., and Goodwin, D.G. (2005). Modeling elementary heterogeneous chemistry and electrochemistry in solid-oxide fuel cells. J. Electrochem. Soc. *152*, A2427.

56. Shi-zhong, W., and Jie, G. (2006). High performance Ni-Fe-lanthanum gallate composite anodes for dimethyl ether fuel cells. Electrochem. Solid-State Lett. *9*, A395.

57. Caneiro, A., Bavdaz, P., Fouletier, J., and Abriata, J.P. (1982). Adaptation of an electrochemical system for measurement and regulation of oxygen partial pressure to a symmetrical thermogravimetric analysis system developed using a Cahn 1000 electrobalance. Rev. Sci. Instrum. *53*, 1072–1075.

58. Kuhn, M., Kim, J.J., Bishop, S.R., and Tuller, H.L. (2013). Oxygen nonstoichiometry and defect chemistry of perovskite-structured $Ba_xSr_{1-x}Ti_{1-y}Fe_yO_{3-y/2+\delta}$ solid solutions. Chem. Mater. *25*, 2970–2975.